



Numerical and experimental study of soot formation in laminar diffusion flames burning simulated biogas fuels at elevated pressures



Marc R.J. Charest*, Ömer L. Gülder, Clinton P.T. Groth

University of Toronto, Institute for Aerospace Studies, 4925 Dufferin Street, Toronto, Ontario M3H 5T6, Canada

ARTICLE INFO

Article history:

Received 9 October 2013

Received in revised form 8 March 2014

Accepted 18 April 2014

Available online 2 June 2014

Keywords:

Soot formation

High pressure combustion

Biogas diffusion flames

CO₂ dilution

Soot modeling

ABSTRACT

The effects of pressure and composition on the sooting characteristics and flame structure of laminar diffusion flames were investigated. Flames with pure methane and two different methane-based, biogas-like fuels were examined using both experimental and numerical techniques over pressures ranging from 1 to 20 atm. The two simulated biogases were mixtures of methane and carbon dioxide with either 20% or 40% carbon dioxide by volume. In all cases, the methane flow rate was held constant at 0.55 mg/s to enable a fair comparison of sooting characteristics. Measurements for the soot volume fraction and temperature within the flame envelope were obtained using the spectral soot emission technique. Computations were performed by solving the unmodified and fully-coupled equations governing reactive, compressible flows, which included complex chemistry, detailed radiation heat transfer and soot formation/oxidation. Overall, the numerical simulations correctly predicted many of the observed trends with pressure and fuel composition. For all of the fuels, increasing pressure caused the flames to narrow and soot concentrations to increase while flame height remained unaltered. All fuels exhibited a similar power-law dependence of the maximum carbon conversion on pressure that weakened as pressure was increased. Adding carbon dioxide to the methane fuel stream did not significantly effect the shape of the flame at any pressure; although, dilution decreased the diameter slightly at 1 atm. Dilution suppressed soot formation at all pressures considered, and this suppression effect varied linearly with CO₂ concentration. The suppression effect was also larger at lower pressures. This observed linear relationship between soot suppression and the amount of CO₂ dilution was largely attributed to the effects of dilution on chemical reaction rates, since the predicted maximum magnitudes of soot production and oxidation also varied linearly with dilution.

© 2014 The Combustion Institute. Published by Elsevier Inc. All rights reserved.

1. Introduction

Virtually all practical combustion devices burn high carbon-content fossil fuels such as coal, petroleum and natural gas. However, conventional sources of petroleum and natural gas are rapidly declining [1]. Additionally, fossil fuel combustion is responsible for nearly all of the anthropogenic emissions of nitrogen oxides (NO_x), carbon dioxide (CO₂), carbon monoxide (CO), soot, aerosols, and other chemical species that are harmful to human health and the environment. Gaseous biofuels, or biogas, are an attractive option to replace fossil fuels since they are environmentally friendly and can be produced locally [2]. They are also renewable, biodegradable, and generate exhaust gases of acceptable quality [3].

Biogases are produced in a variety of environments such as landfills, waste water treatment plants and biowaste digesters

[4]. They typically consist of significant concentrations of methane (CH₄), carbon dioxide (CO₂) and nitrogen (N₂). Biogases are of particular interest because of their significant concentrations of CO₂ and/or N₂, both of which suppress soot formation in pure hydrocarbon flames [5–10]. The addition of inert gases such as CO₂ and N₂ to pure hydrocarbons reduces soot formation by reducing concentrations (dilution effect) and flame temperatures (thermal effect) [10–13]. Carbon dioxide also plays a chemical role by participating in reactions related to soot formation, providing an additional mechanism to suppress soot formation [11,12].

Most practical combustion devices, such as gas turbine combustors and diesel engines, employ high-pressure turbulent flames. These types of flames are not easily characterized because of experimental limitations related to optical accessibility [14], complex flame geometries, and the vast range of time and length scales. As such, laminar flames with simple configurations are commonly studied. However, there are relatively few detailed fundamental studies on soot formation in laminar flames of biogases

* Corresponding author.

E-mail address: charest@utias.utoronto.ca (M.R.J. Charest).

or fuels with similar compositions [5,11,12,15–19]. Furthermore, these studies were all carried out under atmospheric pressure, which does not accurately represent the conditions inside practical combustion equipment.

Pressure profoundly influences the structure and sooting characteristics of laminar diffusion flames through its effects on buoyant forces and chemical kinetics [9,20]. Since the buoyant acceleration scales with pressure-squared, increasing pressure drastically alters the shapes and sooting characteristics of flames [14,21–28]. As such, systematic fundamental studies of simple, small-scale premixed and non-premixed laminar flames are essential in order to develop the accurate physical models necessary to study high-pressure turbulent flames. The knowledge and detailed modeling of these laminar biogas flames, for which the full range of scales can be resolved, serves as a basis for the development of more practical turbulent combustion models.

Recently, several studies have focused on the effects of diluents on processes relevant to soot formation at elevated pressures. Yelverton and Roberts [29] investigated the effect of various diluents – N_2 , Ar, He and CO_2 – on the smoke point heights of laminar methane- and ethylene-air flames between 1 and 8 atm. They found that smoke point heights increased with dilution at atmospheric pressure, but were insensitive to dilution at elevated pressures. The study also emphasized a diluent's effect on entrainment and mixing via changes in kinematic viscosity, which is more important in some cases than its effect on the heat capacity or chemical kinetics. Abhinavam Kailasanathan et al. [30] extended this study by measuring the effects of the same diluents on soot precursor formation and temperature in laminar ethylene-air diffusion flames at similar pressures (i.e., 1–8 atm). The study confirmed the superior soot suppression qualities of CO_2 as compared with the other diluents, even at elevated pressures. However, no measurements of soot concentrations were made in either of the two studies, and the maximum pressure considered was only 8 atm. Practical combustion devices such as gas turbine combustors or diesel engines operate at much higher pressures.

In the present study, the effects of composition and pressure on the structure and sooting propensity of methane-based, biogas-air laminar coflow diffusion flames were investigated. In particular, two different simulated biogas mixtures were examined through a combination of experimental and numerical means and compared with previous results obtained for pure methane-air flames [28,31]. Pressures ranging from 1 to 20 atm were considered.

2. Experimental methodology

The experimental apparatus, described in detail elsewhere [24,31–33], consists of a coflow burner installed inside a pressure vessel. It was designed to allow the burner operating pressure to be varied independently of the surrounding ambient conditions. The burner consists of an inner stainless steel fuel tube with a 3 mm inner diameter and an outer concentric air tube with a 25.4 mm inner diameter. The outer surface of the fuel tube was chamfered to form a knife edge at the nozzle exit plane, which was necessary to improve flame stability over a wide range of pressures. A chimney was also installed to improve flame stability by shielding the core flow from disturbances created inside the chamber.

The spectral soot emission (SSE) diagnostic technique was used to construct radial profiles of temperature and soot volume fraction at different axial heights along the burner axes [34]. In SSE, line-of-sight emission from soot is first measured along chords through the flame at various heights, and radially resolved emission rates are obtained using an Abel inversion procedure [35]. Temperature and soot volume fraction are then computed from

these emission rates. Details of the inversion process and the theory applied to obtain temperature and soot volume fraction from the line-of-sight measurements are described by Snelling et al. [34].

In the current diagnostic setup, the flame was imaged using an achromatic doublet lens with a focal length of 300 mm and an f -number of $f/48$, positioned to provide a 1:1 magnification. It was imaged onto the entrance of a spectrometer and the output was focused onto a 16-bit charge-coupled device (CCD) detector (1340 by 400 pixels). The entrance of the spectrometer contains two slits: a vertical slit 25 μm in width, and a horizontal slit 290 μm in height. The apparatus has a horizontal and vertical spatial resolution of 70 and 290 μm , respectively. Soot emission was measured over the wavelength range from 690 to 945 nm. More details of the experimental setup are provided in [24,31–33].

A majority of the uncertainty in the experimental measurements for soot volume fraction and temperature result from assumptions that were made about the optical properties of soot, i.e., the dimensionless soot refractive index function, $E(m_i)$, where m_i is the complex refractive index of soot at the wavelength λ . The magnitude and variation of this function with λ must be known to estimate the soot volume fraction and temperature from the flame's emission [34]. Although there is a considerable amount of information about the optical properties of soot (see, for example, [36–38]), there is no real consensus on the topic [39]. Snelling et al. [34] compared SSE measurements for an ethylene diffusion flame with two-dimensional line-of-sight light attenuation (LOSA) measurements for soot concentration and coherent anti-Stokes Raman spectroscopy (CARS) measurements for temperature, and found that a constant refractive index function, $E(m_i) = 0.26$, provided the best agreement. These authors demonstrated that changing $E(m_i)$ from a constant function to a linear one that increased at a rate of 40%/ μm resulted in a 3% increase in temperature and a 30% decrease in soot concentration. This represents an extreme case, since a linear regression of the experimental data for $E(m_i)$ published by Krishnan et al. [38] yields a trend line with only 5%/ μm variation in $E(m_i)$. Here, a constant function with $E(m_i) = 0.274$ was chosen based on the recommendations of Thomson et al. [24].

An uncertainty analysis was conducted by Thomson et al. [24] for a similar experimental setup. Based on this analysis, the uncertainty of the temperature and soot volume fraction measurements are 3.5% and 35–40%, respectively, both with a 95% confidence interval. This was confirmed for the current experimental apparatus by Karataş et al. [40]. More details of the uncertainty analysis for the SSE measurements are provided in [41].

Flames of two different methane/carbon dioxide biogas mixtures were investigated, hereafter referred to F20 and F40, and compared with pure methane flames, hereafter referred to as F0. The methane flames were previously studied by Joo and Gülder [31] and Charest et al. [28] over a range of pressures between 1 and 60 atm. Table 1 lists the compositions and total fuel mass flow rates for the three fuels.

For all the flames, constant mass flow rates for methane and air of 0.55 mg/s and 0.2 g/s were maintained, respectively. CO_2 was added to the methane fuel in the F20 and F40 flames, but the methane flow rates were not changed. Pressure varied between 1 and 20 atm; experiments were performed at 1, 5, 10, 15 and 20 atm. Experimental measurements for soot volume fraction and temperature were obtained in height increments of 0.5 mm and radial increments of 50 μm . However, because of low soot levels at lower pressures, reliable measurements could only be made by the SSE system at pressures of 5 atm and above in the F20 flames and 10 atm and above in the F40 flames. The SSE diagnostic technique relies on radiation emitted by soot only. Thus, measurements cannot be made in non-sooting flames. Measurements for the F20 and

Table 1
Chemical composition (percent by volume) of fuels, total fuel mass flow rates, and pressures considered. The experimental and numerical results for F0 at 1, 10, 20, ..., 60 atm were originally presented by Joo and Gülder [31] and Charest et al. [28], respectively. New calculations of the F0 flames at 1, 5, 10, 15, and 20 atm were performed for this study.

Fuel	CH ₄	CO ₂	Mass flow (mg/s)	Pressures (atm)	
				Experiments	Calculations
F0	100	0	0.55	10, 20, ..., 50, 60	1, 5, 10, 15, 20, 30, ..., 50, 60
F20	80	20	0.92	5, 10, 15, 20	1, 5, 10, 15, 20
F40	60	40	1.55	10, 15, 20	1, 5, 10, 15, 20

F40 flames were compared with those obtained by Joo and Gülder [31] for pure methane flames (F0). The pressures considered for each fuel are summarized in Table 1.

3. Numerical model

The numerical framework developed by Charest et al. [42] for the solution of laminar reacting flows with complex chemistry, non-gray radiative heat transfer and soot was applied to study the flames of interest. This computational framework for laminar flames was previously applied to study the effects of both high pressure and low gravity on flame structure and sooting propensity for several gaseous fuels [26–28]. It solves the conservation equations for continuous, multi-component compressible gas mixtures with soot. Soot was modeled using the approach proposed by Leung et al. [43] and Fairweather et al. [44], which describes the evolution of soot through four basic steps – nucleation, surface growth, coagulation and oxidation – and assumes that acetylene is the only precursor responsible for the presence of soot. Surface growth was assumed proportional to the square root of soot particle surface area per unit volume of aerosol. Based on the work of Liu et al. [14,45], this soot model was updated to include oxidation via OH and O as the original model only accounted for oxidation via O₂. All rate constants related to soot were taken from [14]. Multi-species diffusion was modeled using the first-order Hirschfelder et al. approximation [46]. Soot particle thermophoresis was included using a model based on the limit of free-molecular flow [47,48].

Although more advanced soot models based on moment [17,49–51] or sectional [48,52–54] representations have been used to study similar flames, they are too computationally demanding for large parametric studies such as the one performed here. The two-equation model requires much less computational effort, and was shown to provide reliable results for the types of high-pressure flames studied here [14,26–28].

The governing equations were solved numerically using a finite-volume scheme developed by Groth and co-workers [42,55–59]. The scheme uses a piecewise limited linear reconstruction and an approximate Riemann solver to determine the inviscid fluxes [60]. Viscous fluxes were evaluated using the second-order diamond-path method developed by Coirier and Powell [61]. Both the inviscid fluxes and the temporal derivatives were preconditioned using the proposed matrix of Weiss and Smith [62]. This preconditioning helps reduce excessive dissipation and numerical stiffness that is commonly encountered when applying the compressible gas equations to low-Mach-number flows. The fully-coupled, non-linear ODEs were relaxed to a steady-state using the block-based parallel implicit algorithm developed by Northrup and Groth [57] and Charest et al. [42], which makes use of a matrix-free inexact Newton–Krylov method.

Radiation emitted and absorbed by both the gas and soot was modeled using the discrete ordinates method (DOM) coupled with the point-implicit finite volume approach of Carlson and Lathrop [63]. Spatial derivatives were evaluated using centered differences. Ordinate directions and weights were selected based on the T_3

quadrature set [64]. Spectral absorption coefficients for H₂O, CO₂ and CO were approximated using a wide-band model based on the statistical narrow-band correlated- k (SNBCK) model [65,66]. The spectral absorption coefficient for soot was determined based on the Rayleigh limit for small spherical particles [45].

Thermodynamic and transport properties, along with gas-phase kinetic rates, were evaluated using CANTERA [67], an open-source software package for chemically-reacting flows. The simulations were performed using the Gri-Mech 3.0 mechanism for CH₄ combustion [68]. This mechanism was selected because of its relatively small size, i.e., 53 species 325 reactions, and good performance for laminar coflow methane-air flames over a wide range of pressures [14,28].

Calculations were performed for each fuel and pressure considered. The specific operating conditions investigated numerically are summarized in Table 1. Solutions for the pure methane-air flames, originally reported by Charest et al. [28], were re-computed at 1, 5, 10, 15, and 20 atm to match the pressures studied herein.

3.1. Computational domain and discretization

The two-dimensional, axisymmetric computational domain and boundary conditions used to model the coflow burner are shown schematically in Fig. 1. The domain extends radially outwards 12.7 mm to the walls of the chimney and 40 mm downstream. It was also extended 5 mm upstream into the fuel and air tubes to account for the effects of fuel preheating and better represent the inflow velocity distribution [69]. Increasing the size of the domain further had no effect on the accuracy of the solutions. As shown in Fig. 1, the chamfered edge of the fuel tube was approximated by a tube with 0.4 mm uniformly-thick walls. This simplified representation of the fuel tube geometry was employed to reduce the numerical complexity of the problem.

The computational domain was subdivided into 192 cells in the radial- and 320 cells in the axial-direction, respectively. These cells

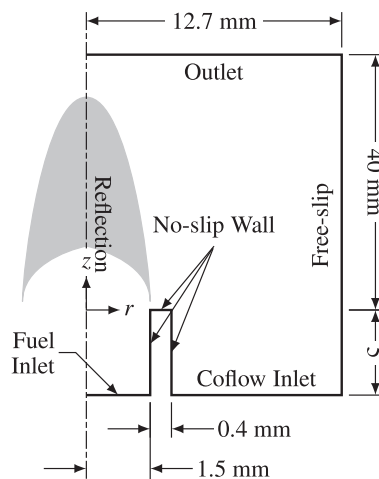


Fig. 1. Computational domain and boundary conditions.

were clustered towards the burner exit plane to capture interactions near the fuel tube walls and towards the centerline to capture the core of the flame. The same mesh was employed for all calculations. Increasing the mesh resolution did not significantly improve the numerical solution.

3.2. Boundary conditions

The far-field boundary was treated using a free-slip condition. At the outlet, temperature, velocity, species mass fractions and soot number density were extrapolated while pressure was held fixed. The mixture composition, velocity, and temperature were prescribed at the inlet while the upstream pressure was extrapolated from inside the domain. Uniform velocity and temperature profiles were applied for both the fuel and air inlet boundaries. The temperatures of the fuel and air supplied to the burner were assumed to be equal to 300 K for all cases. The three surfaces that lie along the tube wall were modeled as solid walls with a zero-slip condition.

For the solution of the radiative transport equation, all boundaries except for the axis of symmetry and the tube walls were assumed to be cold (300 K) and black. The tube walls were also assumed to be black; however, their local temperature varied with the adjacent gas temperature.

All of the flames considered in this study are stabilized by the burner tube rim. As a result, significant heat transfer occurs between the flame and tube that causes the temperature of the tube surface to increase. This heat transfer intensifies with increasing pressure as the flame base moves towards the burner rim and temperature gradients near the burner steepen [24]. Gülder et al. [70] measured temperatures along the burner surface of similar atmospheric laminar diffusion flames that were as much as 100 K higher than the surrounding ambient conditions.

When modelling laminar coflow ethylene–air flames, Guo et al. [69] accounted for gas-tube heat transfer by specifying an experimentally determined temperature distribution along the tube walls. Compared to using fixed temperature walls, their predictions for temperature and soot volume fraction improved when the experimental temperature distribution was prescribed. In Guo et al.'s study, the prescribed experimental temperature distribution was based on the measurements of Gülder et al. [70] for the same flame. However, experimental data for the tube temperature is not available for the flames studied here and the measurements obtained by Gülder et al. [70] are not applicable. Temperatures along the tube wall are expected to be much larger in the present study, especially at higher pressures, since the flame almost touches the burner rim [24,31].

In a previous study of ethylene–air flames by Charest et al. [27], the influence of the wall boundary condition for temperature was found to increase with pressure. Predictions using both fixed-temperature (300 K) and zero-gradient (adiabatic) assumptions were compared, and experimental measurements for soot volume fraction were found to lie between the two sets of predictions. For these ethylene–air flames at 5 atm, a 120 K increase in temperature produced a factor of 2.4 increase in the maximum soot volume fraction.

To account for gas-tube heat transfer in the present study, a Robin-type boundary condition was prescribed for the tube wall temperature. Both a fixed temperature of 300 K and a zero-gradient condition were prescribed with equal weighting. Specifying cold walls represents the limit in which absolutely no heating of the tube occurs, whereas an adiabatic condition represents the opposite limit for the effect of gas-tube heat transfer (i.e., the tube is allowed to heat up to the maximum possible temperature). This boundary condition represents an arithmetic average between the two limits.

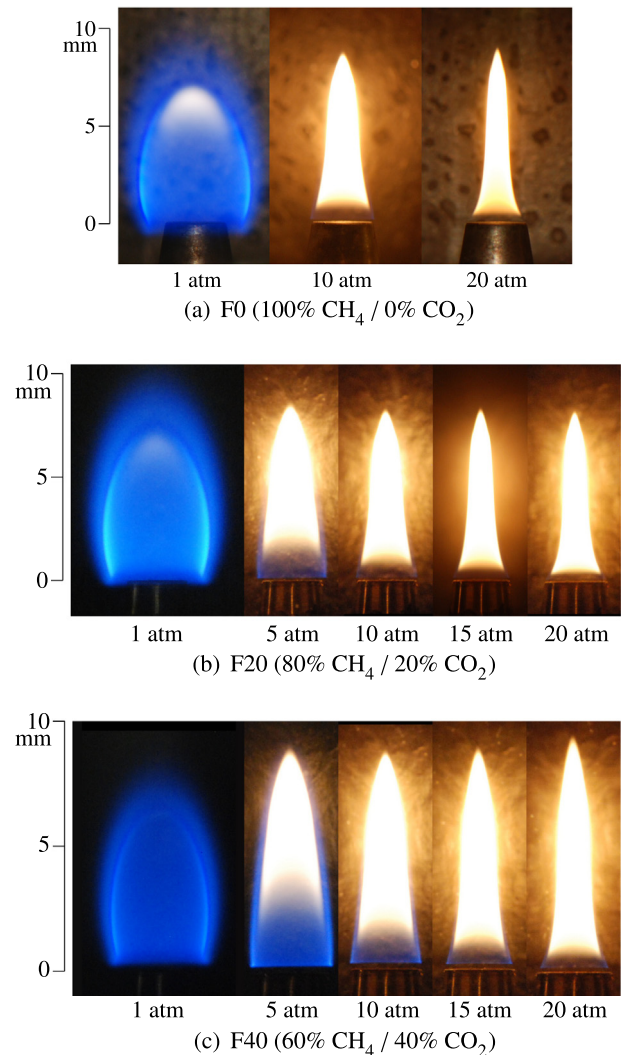


Fig. 2. Experimental images of the methane- and biogas-air flames. The images for the methane-air flames were obtained by Joo and Gülder [31].

4. Effects of fuel composition and pressure

4.1. Overall appearance

In Fig. 2, experimental images of the biogas flames are compared with the results for pure methane flames obtained by Joo and Gülder [31]. The flame heights of both the F20 and F40 flames were almost constant; they were approximately 9 mm between 5 and 20 atm. Although the pure methane-air flames (F0) were not studied at 5 atm, Joo and Gülder [31] observed a constant visible flame height of approximately 9 mm for pressures ranging from 10 to 100 atm. Dilution did not appear to have a significant effect on flame diameter either, especially for pressures of 5 atm and above. Some minor changes in visible shape occurred with dilution at 1 atm, but it was difficult to define the visible edge of these flames due to their low luminosity.

Overall, the shape of the biogas flames and their appearances changed significantly with pressure. Increasing pressure caused the diameter of the biogas flames to narrow and the luminosity to intensify. This is the same behavior that was demonstrated by the pure methane flames. At 1 atm, all three flames possessed a blue region in the lower portion of the flame which got larger as the level of CO₂ dilution was increased. As pressure was increased to 20 atm, this blue region vanished and the yellow luminous

region in the upper portion of the flame moved towards burner tip. The size of the blue zone at the flame's base was always larger for flames with higher CO_2 concentrations in the fuel mixture.

For all three sets of flames, there was a small increase in flame height as pressure was initially increased above 1 atm. This phenomenon was investigated by Charest et al. [27,28] and attributed to increasing rates of air entrainment into the flame.

4.2. Soot volume fraction

As mentioned in Section 2, measurements for soot could only be obtained at pressures of 5 atm and above for the F20 flames, and 10 atm and above for the F40 flames. Soot was predicted to form in all of the flames except for the F40 flame at 1 atm. For this particular flame, the numerical model predicted a highly lifted flame with a liftoff height of approximately 10 mm and negligible soot concentrations. This lifted behavior occurred because the flame could not attach to the burner wall, which was a result of errors in the tube wall boundary conditions. To verify this, additional calculations were performed using a zero heat-flux boundary condition along the tube walls (not provided in this study), and they predicted a flame anchored to the tube walls. As such, the present boundary condition for the temperature along the burner tube walls represents a compromise to obtain accurate and stable solutions over a wide range of pressures. While it introduces some errors in the predicted solutions at lower pressures, it yields more accurate predictions and stable flames at high pressures.

Radial profiles of the measured soot volume fraction for the biogas flames at various heights above the burner are provided in Fig. 3. Although measurements were made by scanning the entire flame's diameter, the experimental data in the figure represents averages of the left and right side scans. As observed in Fig. 3, soot volume fraction increased significantly when pressure was

increased, and the location where the radial profiles peaked moved towards the centerline. By increasing pressure from 10 to 20 atm, the maximum measured soot concentrations increased from 8 to 29 ppm (a factor of 3.6) in the F20 flames, and from 1 to 9 ppm (a factor of 9) in the F40 flames. In comparison, they increased from 15 to 53 ppm (a factor of 3.5) in the methane-air flames studied by Joo and Gülder [31]. Thus, the relative increase in maximum soot volume fraction with pressure increased with CO_2 dilution, mainly because CO_2 dilution causes the flames to behave like lower-pressure pure methane flames. Lower pressure flames are more sensitive to increases in pressure [24,28,31].

In the experiments for both biogas flames, soot first appeared in an annular ring near the burner rim and increased in concentration further up in the flame. This annular distribution disappeared near the tip of all the biogas flames when the “wings” of the distribution converged towards the centerline. This behavior of the two biogas flames is similar to previous observations for pure methane-air diffusion flames [24,31].

The predicted radial profiles for soot volume fraction are also presented in Fig. 3. The model predicts many of the experimentally-observed trends, but generally under-predicts soot volume fractions for all pressures investigated, especially near the centerline in the upper portion of the flame. In some cases, the predictions were as much as 250–300% above or below the measurements. Although these discrepancies are large, the simplified soot model predicts the correct trends with pressure and dilution, i.e., dilution suppresses soot formation while increasing pressure enhances it. Thus, the simplified soot model would seem suitable for the current study.

Two-dimensional contour plots of soot volume fraction for the methane and biogas flames were constructed from the experimental measurements and are compared with the numerical results in Fig. 4. Qualitatively, the predicted and measured flame geometries

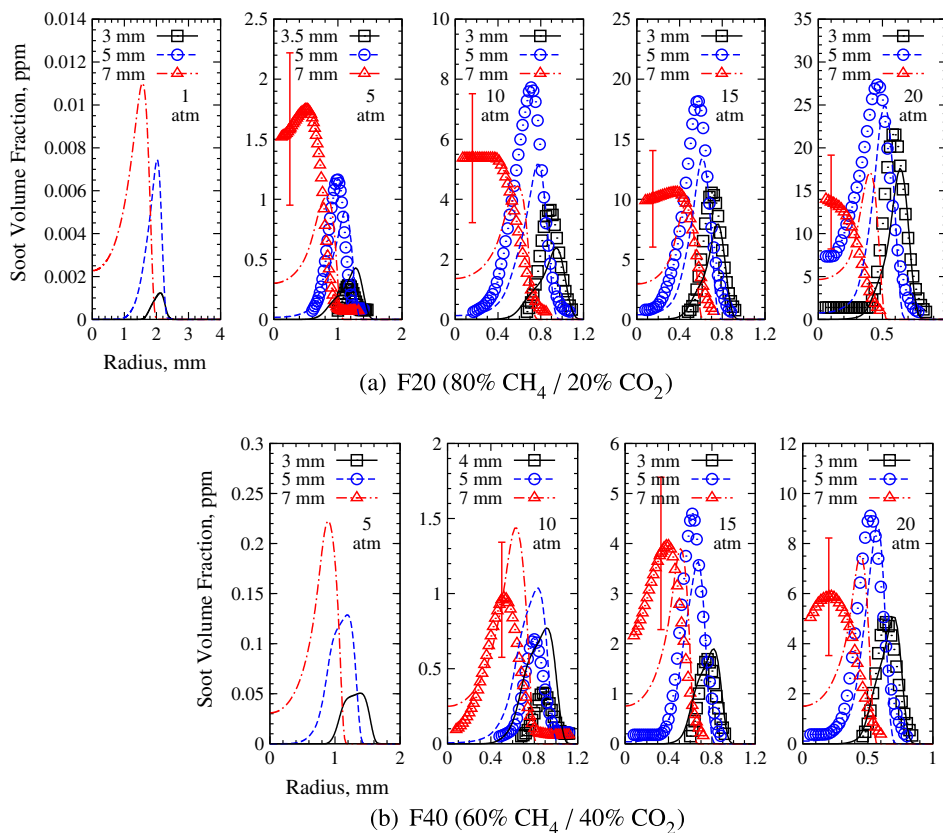


Fig. 3. Effect of pressure on the predicted and measured radial soot volume fraction profiles for the biogas flames. The error bars correspond to 40% of the measured value.

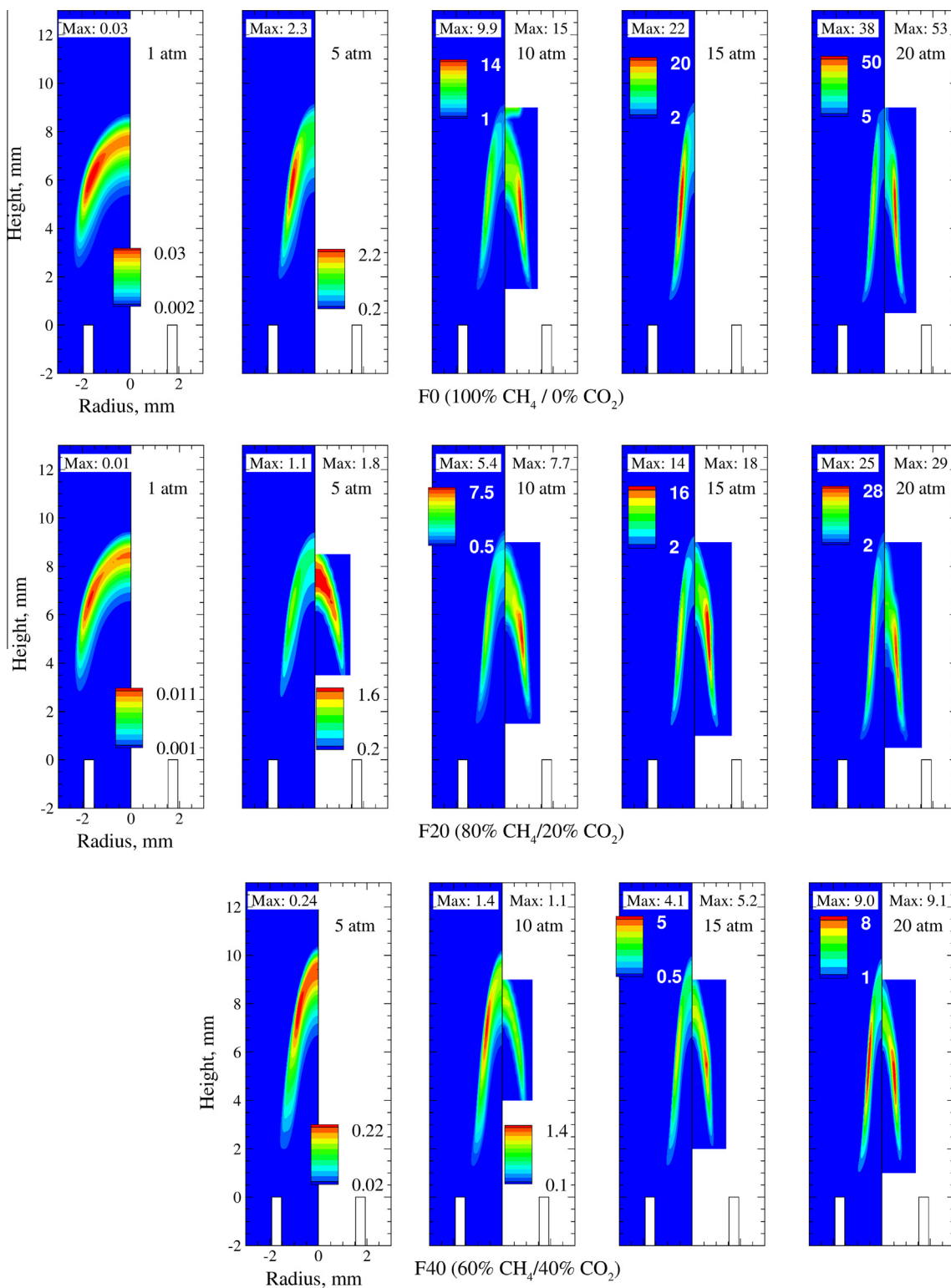


Fig. 4. Contours for soot volume fraction in the (top) F0, (middle) F20, and (bottom) F40 flames. In each panel, the predictions are plotted on the left of the centerline while the experimental measurements are plotted on the right. The maximum soot concentrations are indicated in each panel. Units are in ppm. The experimental data for the methane-air (F0) flames were originally published by Joo and Gülder [31].

were similar and the narrowing of the flame with increasing pressure was clearly observed in both sets of results. Here, the isocontour corresponding to a soot volume fraction equal to 0.001 ppm was used to mark the edge of the flame. Since the soot volume fraction drops off rapidly near the edge, any concentration close to zero

could have been chosen to locate the edge of the flame with negligible effect on the results.

At the lowest pressure that measurements could be made for each biogas flame, maximum soot concentrations occurred near the tip of the flame along the centerline. However, the overall

structure of the measured soot distribution changed for both bio-gas flames when pressure was increased. At higher pressures, the experimental measurements for soot volume fraction had a more pronounced annular structure and the maximum concentrations occurred in the annular region near the flame's mid-height. This annular structure was more pronounced and thinner at higher pressures. The numerical model also predicted this transition to an annular soot distribution as pressure was increased; however, the transition was predicted to occur at lower pressures. For example, the transition was observed to occur in the experiments for the F40 flames between 10 and 15 atm, but the numerical model predicted a transition between 5 and 10 atm.

The model predicted the height at which soot formation began with a reasonable degree of accuracy. However, as observed in Fig. 4, the numerical model predicted the onset of soot formation slightly lower in the flame than observed in the experiments, especially at lower pressures. The model predicted the onset of soot formation at a height of 2.7 mm in the 5 atm F20 flame, compared to the measured value of approximately 3.5 mm, and at a height of 1.9 mm in the 10 atm F40 flame, compared to the measured value of approximately 4.0 mm. The predictions were better at higher pressures. At 20 atm, the predicted and measured heights at which soot was first observed were 0.9 and 1.0 mm for the F20 flame, respectively, and 1.0 and 1.5 mm for the F40 flame, respectively. However, measurements cannot reliably detect soot concentrations below 0.1–1.0 ppm. Nonetheless, both the experiments and predictions show that soot formation began lower in the flame with increasing pressure, and diluting the fuel stream with CO₂ moved the height where soot formation began downstream. The latter effect became less pronounced as pressure was increased.

4.3. Temperature

Despite the errors in the predicted soot volume fraction, the computed radial temperature profiles given in Fig. 5 agree quite well with the measurements. Three axial locations were chosen for this comparison: low in the flame where soot particles undergo nucleation and growth, the middle of the flame near the maximum soot volume fraction, and higher in the flame where soot is oxidized. Note that experimental measurements for temperature are only available in locations where soot is present. This is because the SSE diagnostic technique relies on radiation emitted by soot only.

Similar relationships between pressure, flame height, and temperature are observed in both the numerical predictions and experimental measurements. In all flames, the temperatures closer to the centerline were somewhat under-estimated (by as much as 125 K) while the peak temperatures tended to be over-estimated, especially at higher pressures. For example, the peak temperature 3 mm above the burner in the 20 atm pure methane-air flame was over-predicted by approximately 250 K. The predicted temperatures in the peaks of the radial profiles actually increase slightly with pressure for each height, which contradicts the experimental measurements. These observed discrepancies for temperature do not explain the errors in the computed soot volume fraction. Discrepancies in the predicted peak soot volume fractions displayed the opposite behavior; they decreased with increasing pressure. As such, the errors are associated with the currently employed models for soot and radiation heat transfer, as well as the tube wall boundary condition.

For all of the flames, the predicted radial profiles of temperature were shifted slightly outward. This resulted from assuming a simplified representation of the burner geometry in the calculations. The outer edge of the burner is chamfered, but this feature was neglected in the numerical model. A tube with a constant wall thickness was assumed instead.

An important experimental observation is that the peak values of the measured radial temperature profiles, which occurred in the “wings” of the flame, increased with height. The magnitude of this increase became more prominent as pressure was increased, but it decreased with dilution. Although the predictions also indicate that the maximum temperatures occurred in the “wings” of the flame, the magnitudes were predicted to decrease with flame height. A slow increase in temperature with height is expected for highly sooting flames since heat is released through the oxidation of soot. However, the numerical model failed to capture this phenomenon. The model did manage to capture the fact that the changes in peak temperatures with flame height got smaller with dilution.

The predicted temperature contours for the three sets of flames are compared in Fig. 6. The lifted 1 atm F40 flame that was mentioned in Section 4.2 is also visible in the figure. This prediction of a lifted F40 flame at 1 atm does not agree with the experimental observations depicted in Fig. 2 and was attributed to uncertainties in the tube wall boundary conditions. Since the 1 atm F40 flame lifts off of the tube, its predicted gas temperatures were significantly lower than the F0 and F20 flames at the same pressure. For 5 atm and above, the decrease in peak temperature with dilution was approximately constant for all pressures – a difference of roughly 93–94 K was observed between the F0 and F40 flames at the same pressure. Predicted peak temperatures increased with pressure.

Figure 7 illustrates the predicted temperatures along the centerlines of all the flames investigated. The calculations predicted a reduction in the overall temperatures near the flame tip when the fuel mixture was diluted with CO₂. For all pressures investigated, adding CO₂ lowered temperatures along the centerline, but this reduction got smaller as pressure was increased. The reduction in temperature near the flame tip when methane was diluted with 40% CO₂ was 150 K at 1 atm but only 70 K at 20 atm. The predicted flame temperatures along the centerline of all the flames increased when pressure was increased from 1 to 20 atm, and this increase was more pronounced lower in the flame.

The variation of the measured and predicted maximum flame temperatures with height are illustrated in Fig. 8 for each flame. The calculations predicted a rapid initial increase in flame temperature with height as the fuel was oxidized. This was followed by a gradual decrease in temperature as heat was lost to the surroundings via radiative transfer. Finally, the temperature rapidly decreased above the flame tip as the hot gases mixed with the colder surrounding air. While all of the flames above 1 atm displayed this behavior, the predictions for the 1 atm flames displayed a gradual increase in temperature along the flame's height. This different behavior at 1 atm occurs because reaction rates are slower and radiative heat losses are lower (less soot) [28]. The measured values for the maximum temperatures along the flame are similar in magnitude, but their variation with flame height differs. There was a sharp measured increase in temperatures near the burner rim, which is followed by a steep decrease within the first 2 mm of the flame. Above a height of 2 mm, the measured temperatures gradually increase as soot oxidizes.

In the experiments, the change in the maximum flame temperatures with dilution was smaller than predicted. For example, the measured drop in temperature when methane was diluted with 40% CO₂ was approximately 84 K at 10 atm and 28 K at 20 atm. The corresponding predicted reduction in temperature was approximately 90 K for all pressures except 1 atm. As such, dilution effects on temperature were over-predicted by the calculations.

4.4. Flame shape

The effect of pressure and composition on the radius and length of the flames is illustrated in Fig. 9. Both predictions and

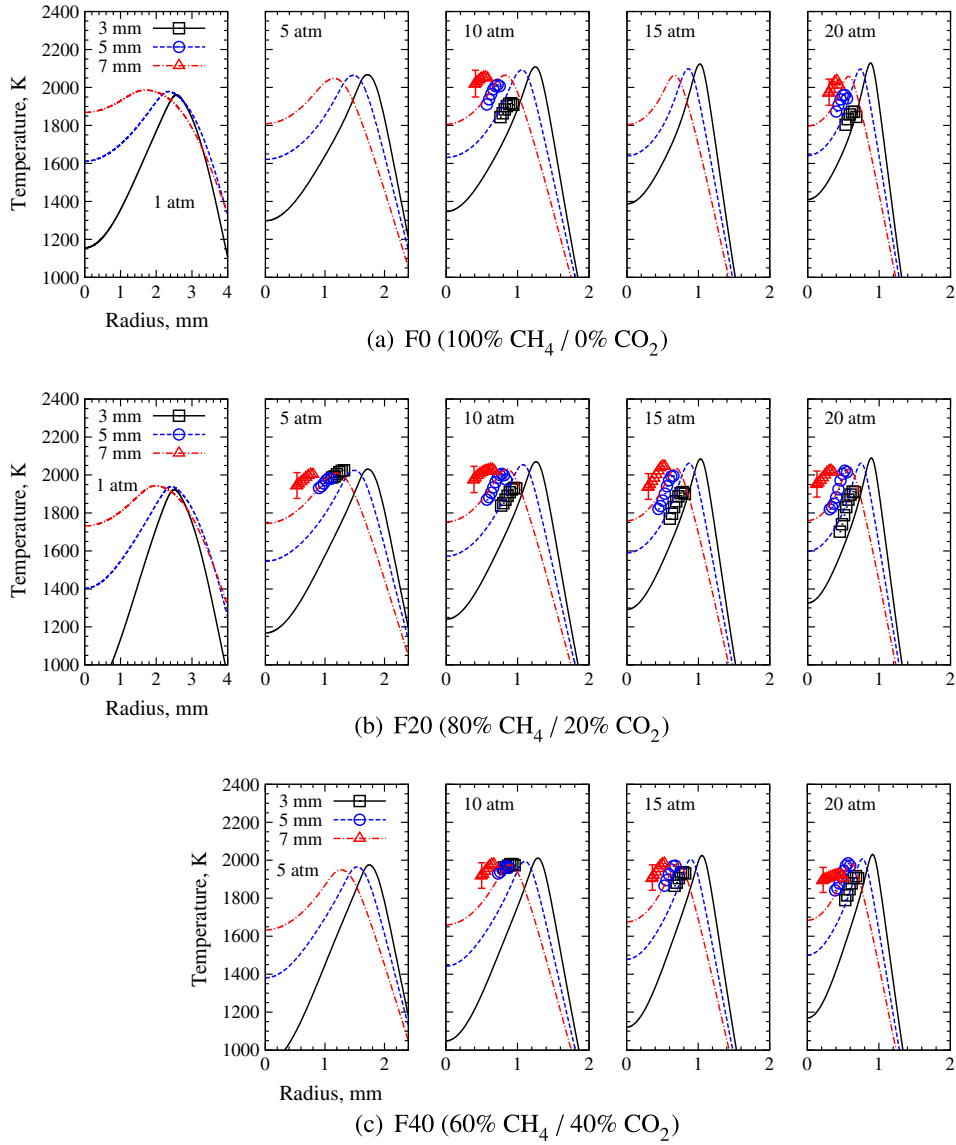


Fig. 5. Effect of pressure on the predicted (lines) and measured (symbols) radial temperature profiles for the methane and biogas flames. The error bars correspond to 3.5% of the measured value. The experimental results for the methane-air (F0) flames were originally published by Joo and Gülder [31].

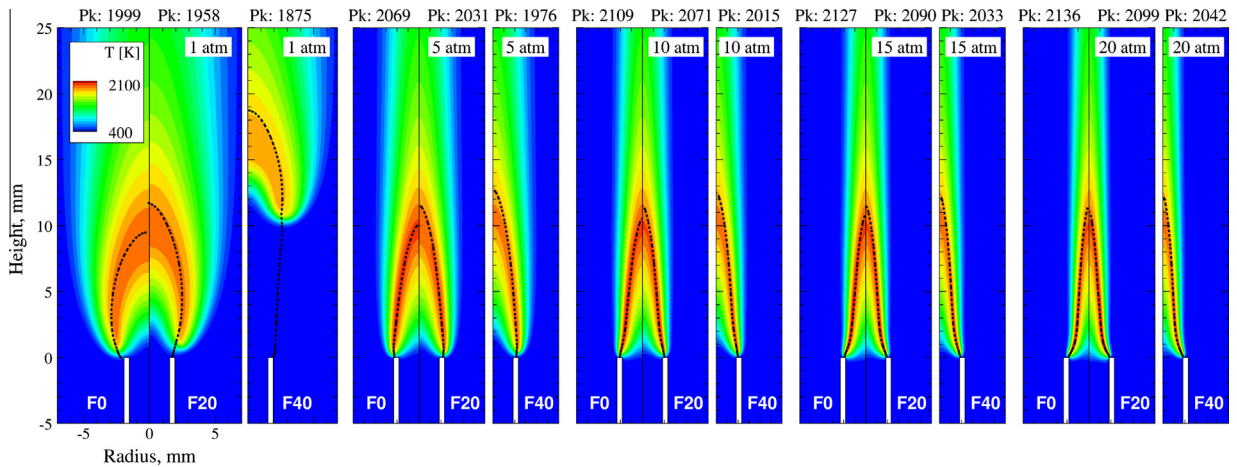


Fig. 6. Predicted temperature contours for the methane and biogas flames. Units in K. The black dashed lines correspond to the location where the mixture fraction is equal to the stoichiometric value. Peak (Pk) values for each flame are also provided in the figure.

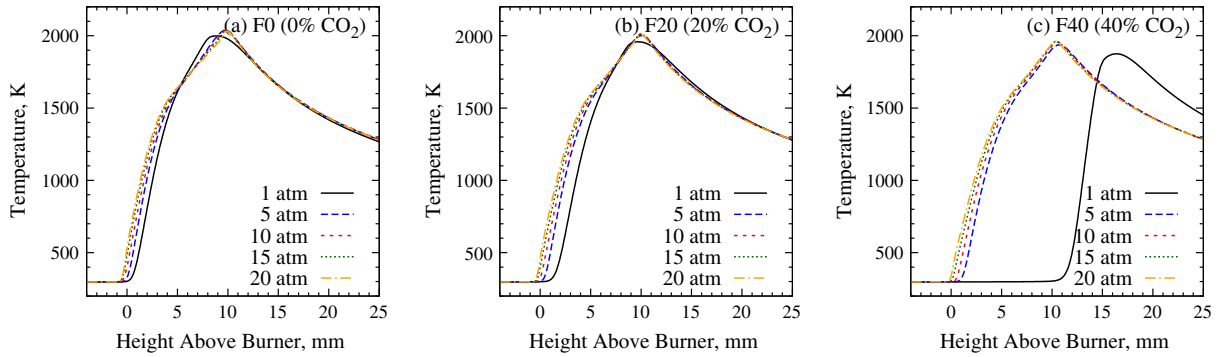


Fig. 7. Effect of pressure and composition on the predicted centerline temperatures.

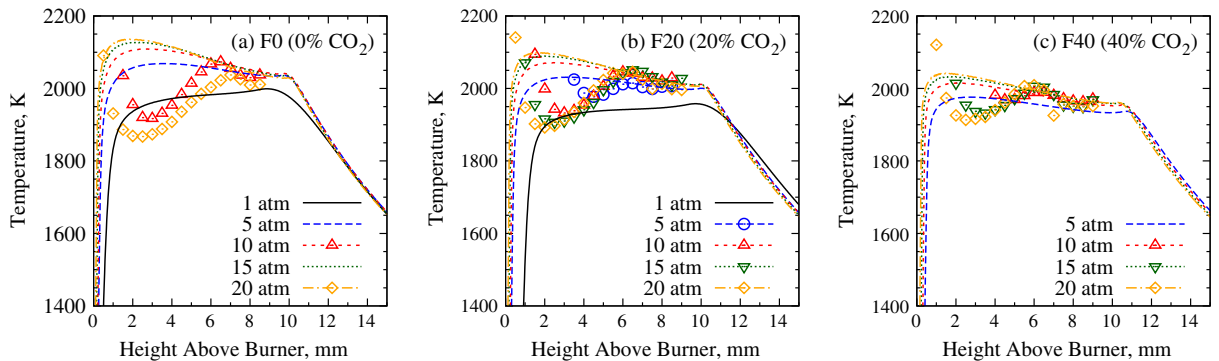


Fig. 8. Effect of pressure and composition on the maximum flame temperatures.

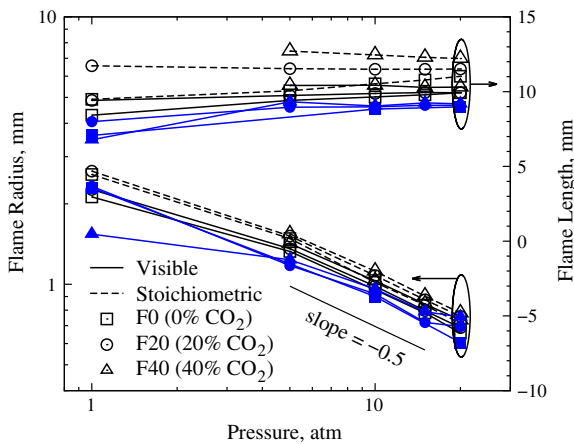


Fig. 9. Effect of pressure and fuel composition on flame shape. Flame radii correspond to an axial height of 5 mm. Open symbols and black lines denote the predictions, while closed symbols and blue lines denote the experimental results.

experimental observations are provided in the figure. For the computational results, the visible flame shape was defined by the isocontour where the soot volume fraction was equal to 0.001 ppm. As already mentioned in Section 4.2, any concentration close to zero could have been chosen since the soot volume fraction drops off rapidly near the edge.

The predicted shape defined by the stoichiometric mixture fraction was also included in Fig. 9. Here, the mixture fraction was computed using the following relation [71]:

$$Z = \frac{Y_C - Y_{C2}}{mM_C} + \frac{Y_H - Y_{H2}}{nM_H} + \frac{Y_{O2} - Y_O}{(m+n/4)M_O} \quad (1)$$

where Y_j and M_j are the mass fractions and atomic masses for the elements of carbon, hydrogen and oxygen. The constants m and n represent the number of carbon and hydrogen atoms in the fuel (C_mH_n). Subscripts 1 and 2 refer to values in the fuel and air streams, respectively.

As observed in Fig. 9, the predictions for flame radius and length are in good agreement with the experimental observations. However, both the flame radius and length were slightly over-predicted in all cases. In both the experiments and predictions, the radius was observed to decrease with increasing pressure according to the relationship

$$r_f \propto p^a \quad (2)$$

where r_f is the visible flame radius, p is the pressure, and a is the pressure exponent. Based on a linear regression analysis, the measured and predicted values of a are -0.41 ± 0.05 and -0.49 ± 0.02 , respectively. This is in accordance with previous findings that $a = 0.5$ [14,23,24,27,28,31,32]. The deviations in the measured value of a from the theoretical value of 0.5 are a result of data scatter and difficulties accurately measuring the visible flame radius.

As observed by the experimental results in Fig. 9, diluting methane with CO_2 had some effect on the flame shape at 1 atm. It decreased the diameter at an axial height of 5 mm by a factor of 1.5 when 40% CO_2 was added to methane. Although, it was difficult to accurately define the visible flame edge in the experimental images (Fig. 2) when there was little to no soot. Any observed effects of dilution completely disappeared when the pressure was increased above 1 atm.

The flame height based on soot volume fraction was accurately predicted over the range of applicable pressures by the model, 9 mm (measured) versus approximately 10 mm (predicted), for all flames between 5 and 20 atm. At 1 atm, the measured flame heights were smaller; they were 7, 8, and 7 mm for the F0, F20,

and F40 flames, respectively. The calculations predicted visible flame heights of 8 mm (F0) and 9 mm (F20) at 1 atm. This slight decrease in visible flame height at lower pressures was also observed by others [24]. As mentioned previously, it occurs because more air is entrained into the flame when pressure is initially increased above 1 atm [27,28].

The predictions for the flame heights of the methane and biogas flames displayed differing trends as pressure was increased. When pressure was increased from 5 to 20 atm, the model predicted a 5% increase in visible height for the F0 flames, a 2% increase in height for the F20 flames, and a 1% decrease for the F40 flames. This fuel-dependent behavior was not observed in the experiments as the measured visible flame heights are roughly constant between 5 and 20 atm. The discrepancies are likely due to the different definitions used to locate the flame's edge (i.e., soot volume fraction or mixture fraction versus visible characteristics).

For the entire range of pressures investigated, the calculations predicted a slight increase in height when the fuel was diluted. This increase was smaller at higher pressures, and it was also much more pronounced for the stoichiometric flame lengths. There was a negligible increase in predicted visible height; it only increased by 10% at 5 atm and 4% at 20 atm when 40% CO₂ was added to methane. The changes in predicted stoichiometric flame lengths were much larger; they increased by 26% at 5 atm and 11% at 20 atm. With the exception of some experimental scatter, no noticeable changes in the measured visible flame height with dilution were observed at pressures above 5–10 atm.

The effects of pressure and dilution on the flame envelope are illustrated in Fig. 10, which compares the predicted stoichiometric mixture fraction isocontours for each flame. At lower pressures, there was a significant effect of dilution. However, at higher pressures, dilution mainly caused the flame to lengthen. Fig. 10 illustrates the differing predicted relationships between flame height and pressure for each fuel that was mentioned previously. The stoichiometric height of the pure methane flames increased with pressure; the height of the F20 flames was roughly independent of

pressure, and the height of the F40 flames actually decreased slightly with pressure.

4.5. Velocity and entrainment

As previously discussed, there were changes in the observed flame height of all three sets of flames as pressure was increased above 1 atm. However, Roper's correlations for buoyancy-dominated laminar jet diffusion flames [72,73] predict pressure-independent flame heights over all ranges of pressures. These correlations assume that the mass flow rate through the flame envelope is constant for constant fuel flow rates, but previous investigations of pure methane and ethylene flames found that this assumption is not valid at low pressures [27,28]. In these previous investigations, Charest et al. [27,28] predicted an increase in the mass flow rate through the flame's envelope as pressure was increased to approximately 5 or 10 atm. It was concluded that these increases in mass flow rate caused the observed increases in flame height with pressure at low pressures.

Figure 11 illustrates the predicted maximum mass flow rate through the stoichiometric flame envelope as a function of fuel composition and pressure. All three fuels investigated – F0, F20 and F40 – entrained more air as pressure was increased above 1 atm. However, above 5–10 atm, further increases in the mass flow through the flame envelope began to get smaller, and so did further increases in flame length. The entrainment completely leveled off after 15 atm for the methane flame, but it still increased slightly with further increases in pressure for the two biogas flames.

The relationship between height and mass flow rate predicted in the present study for the pure methane flames confirms the numerical results obtained by Charest et al. [28], and these numerical predictions correspond with the experimental observations for the heights of the pure methane flames. However, even though the mass flow rates through the two biogas flames increase sharply between 1 and 5 atm, the predicted visible and stoichiometric heights of the F20 flames are roughly independent of pressure, and the predicted heights of the F40 flames actually decrease slightly. As mentioned previously in Section 4.4, these predicted trends for the heights of the two biogas flames do not correspond with the experimental observations. In the experiments, the visible heights of the biogas flames were observed to increase as pressure was increased from 1 to 5 atm. As such, since the predicted relationship between flame height and pressure do not agree with

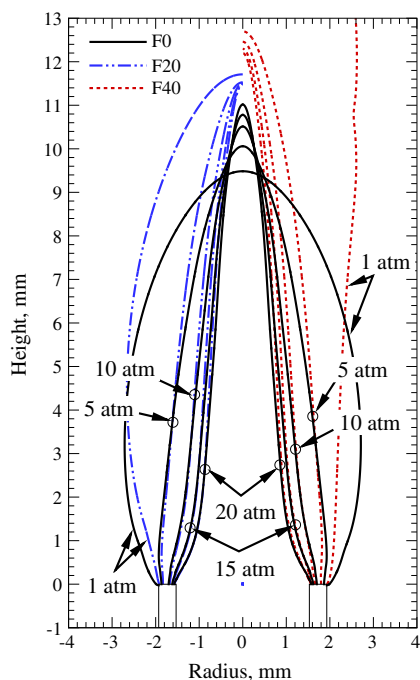


Fig. 10. The effect of pressure and composition on the predicted stoichiometric mixture fraction surface.

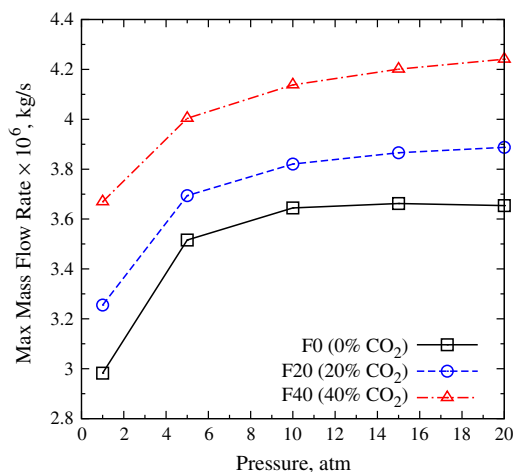


Fig. 11. Predicted maximum mass flow rate through the stoichiometric flame envelope.

the experimental observations at low pressures, it is not clear whether the experimentally observed changes in height of the two biogas flames between 1 and 5 atm can be attributed to changes in the mass flow rate through the flame's envelope.

As observed in Fig. 12, there was a small affect of pressure and dilution on the flame's predicted centerline velocity. For example, considering the F0 flames, the velocity along the centerline at the inlet of the domain (upstream of the burner exit) is approximately 4 times slower at 20 atm than at 5 atm. This is a result of the effect of pressure on density. However, buoyancy forces rapidly accelerate the flow once it leaves the burner nozzle. The centerline velocity of the 20 atm flame rapidly increases above that of the equivalent 5 atm flame. At 5 mm above the burner rim, the centerline velocity of the 20 atm F0 flame is 1.1 times faster than at 5 atm. The same predicted trend was observed for the F40 flames.

Dilution was predicted to have a similar effect to pressure on the flame's centerline velocity. At 5 atm, the centerline velocity near the domain inlet for the F40 flame was 1.6 times faster than that of the F0 flame, which is because of the differences in density and prescribed mass flow rate. Buoyancy accelerates the flow for both 5 atm flames as it leaves the burner nozzle, but the centerline velocity of the F40 flame reaches higher values. At 5 mm above the nozzle exit plane, the centerline velocity of the 5 atm F40 flame is 1.2 times faster than that of the F0 flame at the same pressure. Similar effects of dilution were also predicted at 20 atm, except the centerline velocity of the F40 flame 5 mm above the burner rim was 1.1 times faster than predicted for the F0 flame.

4.6. Soot yield

To assess the fuel's propensity to soot and its sensitivity to pressure, the variation of the carbon conversion factor with pressure was studied. This parameter has been used to quantify the effects of pressure on soot formation by several other researchers (see, for example, [74] and references therein). It is a better measure of sooting propensity, since it measures the total mass of soot produced instead of the concentration.

The carbon conversion factor, η_s , is defined as \dot{m}_s/\dot{m}_c where \dot{m}_c is the carbon mass flow rate at the nozzle exit [22]. The mass flux of soot through a horizontal cross-section is

$$\dot{m}_s = 2\pi\rho_s \int f_v v r dr \quad (3)$$

where $\rho_s = 1.9 \text{ g/cm}^3$ is the density of soot [45], f_v is the soot volume fraction and v is the axial velocity. Since the velocity was not

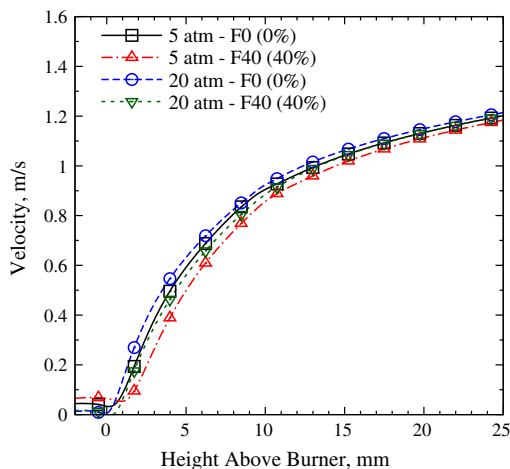


Fig. 12. Predicted axial velocity along the centerline.

known in the experiments, the predicted velocity field was used to estimate the measured η_s . CO_2 was not included in the calculations for \dot{m}_c since it is considered inert. Thus, all sets of flames have the same carbon flow rate at the nozzle, 0.412 mg/s. The experimental results for the maximum carbon conversion factor in the pure CH_4 -air flames (F0) are based on the measurements obtained by Joo and Gülder [31], but the numerical predictions were re-computed to match the pressures of the biogas flames.

The maximum carbon conversion factor, illustrated in Fig. 13, increased with pressure and decreased with amount of CO_2 . The predictions mimicked the experimentally observed trends reasonably well, but the maximum η_s in each flame was always under-predicted, except for the F40 flame at 10 atm. For this particular flame, the maximum η_s was under-predicted by 30%. The maximum η_s for the biogas flames was generally over-predicted by approximately 30–50%. The largest error, i.e., 50%, occurred for the 15 atm F20 flame.

In general, the predictions of η_s for flames with higher measured soot concentrations were worse. This is largely attributed to errors in the simplified soot model that are introduced by the reduced soot chemical kinetics and the monodisperse particle size distribution. Additionally, as soot concentrations rise, the dilute-phase assumption breaks down and volume effects may become important [75].

As observed in Fig. 13, all three sets of flames – F0, F20 and F40 – displayed a similar dependence on pressure which weakened as pressure was increased. However, the flames with higher CO_2 concentrations displayed a stronger relationship between η_s and pressure (i.e., slightly higher slope). This results because CO_2 dilution suppresses soot formation, and there is more carbon available for further production of soot.

Both sets of results, experimental and numerical, indicated that the degree of soot suppression was larger at lower pressures. At 10 atm, the measured carbon conversion factor was reduced by a factor of 14.4 when methane was diluted with 40% CO_2 . In comparison, the mathematical model predicted a reduction of a factor of 6.8 at 10 atm. The measured and predicted reduction in the carbon conversion factor with dilution was a factor of 4.9 and 4.3 at 20 atm, respectively.

As observed in Fig. 14(a), both the measured and predicted maximum carbon conversion factor displayed a linear dependence on the level of CO_2 dilution. The measured and predicted peak soot volume fraction also displays a similar linear dependence on CO_2 dilution, as illustrated in Fig. 14(b). While this linear behavior

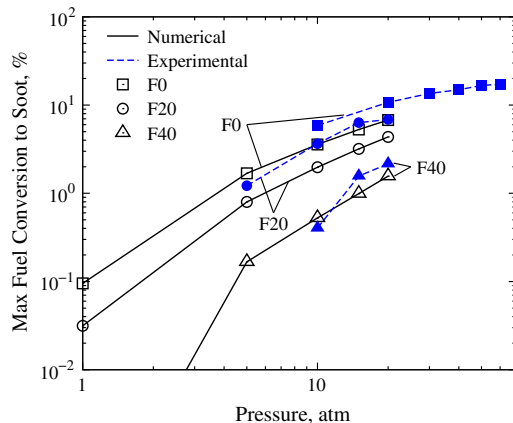


Fig. 13. Effect of pressure and composition on the maximum carbon conversion factor. Open symbols with solid lines denote the predictions and closed symbols with dashed lines denote the experimental results. The experimental results for the pure CH_4 flames (F0) are based on the measurements obtained by Joo and Gülder [31].

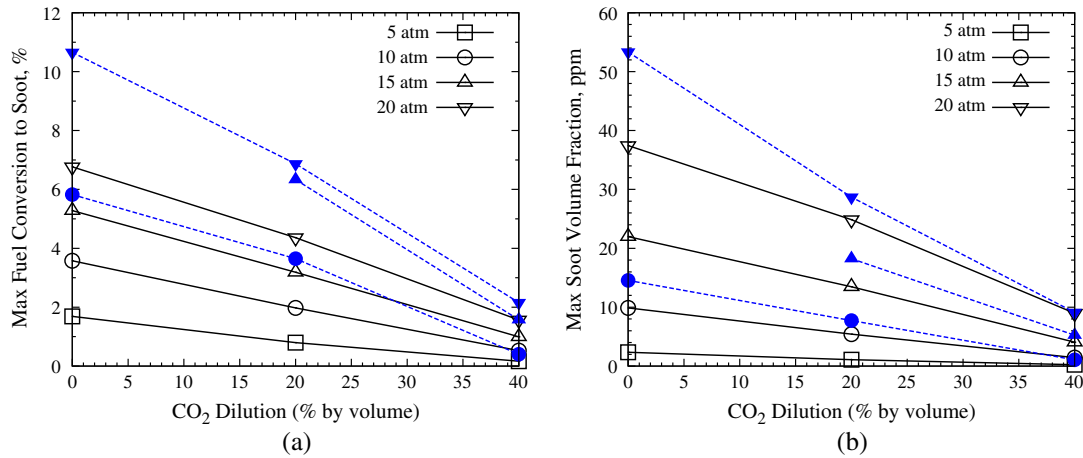


Fig. 14. Measured and predicted (a) maximum carbon conversion factor and (b) as a function of CO₂ dilution. In both figures, open symbols with solid lines denote the predictions and closed symbols with dashed lines denote the experimental results.

was especially prominent in the numerical results, it was hard to clearly identify in the experimental results because of measurement scatter. Nonetheless, experimentally observed deviations from a linear dependence of the carbon conversion factor and soot volume fraction on CO₂ dilution are within the experimental uncertainty quoted in Section 2.

4.7. Production rates

The effect of pressure on the predicted maximum soot production and destruction rates are illustrated in Fig. 15(a). Maximum production rates refer to the largest positive values of the soot mass source term in the flame, whereas maximum destruction rates refer to the smallest negative values. These rates represent the largest magnitudes of the rate of soot production and oxidation/destruction in each flame, and both rates displayed a large dependence on pressure and dilution. They varied with pressure according to a quadratic polynomial, not via a strict power law, and linearly with CO₂ dilution (for a fixed pressure). This is illustrated by the curve-fits in Fig. 15(a). The maximum soot production and destruction rates varied according to following relationships:

$$\text{Max Prod.} = (-0.20 + 0.13p + 0.02p^2) \cdot (1 - 1.82[\text{CO}_2]) \quad (4a)$$

$$\text{Max Dest.} = (0.88 - 0.52p - 0.11p^2) \cdot (1 - 1.67[\text{CO}_2]) \quad (4b)$$

where p is the pressure in atm and $[\text{CO}_2]$ is the percent CO₂ by volume in the fuel stream. Eqs. (4a) and (4b) vary linearly with CO₂ concentration and quadratically with pressure.

Increasing the dilution altered the relationship between soot production and pressure, mainly by delaying its increase with pressure. The magnitude of the soot production rates actually decreased faster with pressure than the magnitudes of the soot destruction rates. This is apparent because the coefficient in front of the p^2 term in Eq. (4b) is larger than in Eq. (4a). Adding a diluent, CO₂ in this case, decreased chemical reaction rates by reducing reactant concentrations and temperatures. Therefore, both soot production and destruction rates were expected to decrease. There was also a secondary effect of dilution in this case. As observed in Fig. 15(b), dilution reduced the predicted acetylene production rates, so less acetylene was available for conversion to soot.

These results, i.e., the linear relationship between dilution and the maximum production/destruction rates, agree with those of Section 4.6 since the measured and predicted overall soot yield varied linearly with the level of dilution (Fig. 14(a) and (b)).

4.8. Soot particle residence time

The predicted soot concentrations along a particle's path are illustrated in Fig. 16. The particle paths chosen, which were constructed from the numerical results, passed through the location

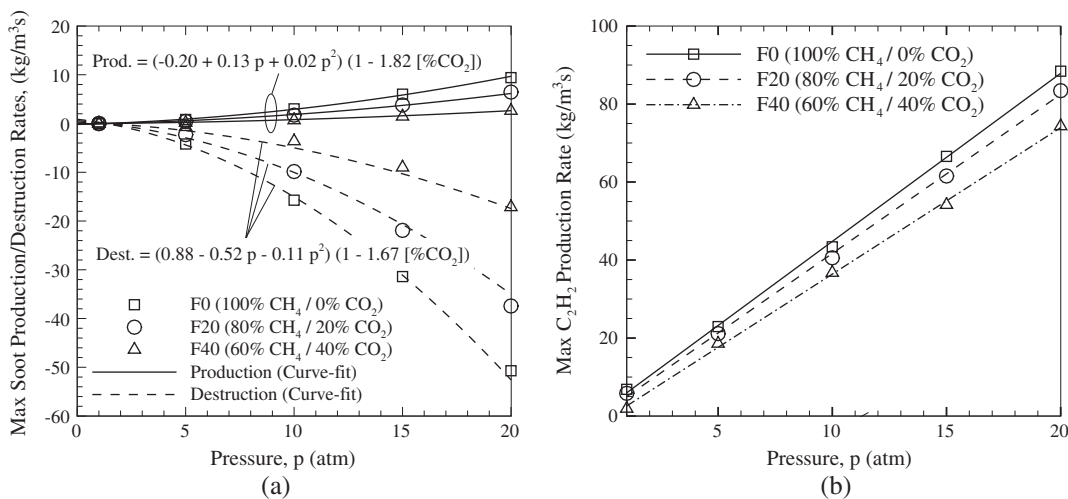


Fig. 15. Effect of pressure on the predicted maximum production and destruction rates of (a) soot and (b) acetylene.

of maximum soot concentration and started when soot formation began (i.e., soot concentrations rose above 0 ppm). While a particular particle whose lifetime begins at the start of the chosen trajectory may not make it to the region of maximum soot concentration, other particles that are nucleated along this trajectory will. As such, this analysis represents a statistical average of all particles nucleated and destroyed along a particular path. Trajectories that pass through any point could have been chosen. The region of maximum soot concentration was chosen here since it represents the most likely trajectory, i.e., it has the highest soot concentrations. A similar analysis was performed in previous investigations [27,28]; however, a different definition for the soot residence time was chosen here.

The overall residence time or lifetime of soot, which is defined as the length of time from the initial formation to complete destruction of soot over the chosen trajectory, is not the same as the residence time of the bulk flow through the flame's envelope. The residence time of the bulk flow is roughly independent of pressure and depends on the fuel mass-flow rate only [9,72,73], as long as the flame is fully developed and pressure sufficiently high [27,28]. However, the average soot particle residence time generally increased with pressure. As pressure was increased, soot was observed lower in the flame in both the measurements and predictions (see Fig. 4), but the visible height of the flame (i.e., the location where soot was fully oxidized) did not change significantly, and neither did the axial velocities along the centerline 2–3 mm above the burner rim.

As illustrated in Fig. 16, pressure and dilution had a significant affect on the overall particle residence times, as well as the relationship between soot concentration and residence time. The increase in soot production rates with pressure, which was observed in Fig. 15(a), caused soot concentrations to rise more quickly along their trajectory. The F0 and F20 flames displayed an increase in overall particle residence time with pressure, while the changes in residence time with pressure were much more complex for the F40 flames. For these flames, the total soot residence time initially increased with pressure up to 10 atm, but began to decrease with further increases in pressure beyond 10 atm.

As with pressure, the relationship between the overall soot residence times and dilution was also complex. Diluting methane with 20% CO₂ shortened the residence times at 20 atm, but further dilution caused residence times to increase. At 5 atm, however, dilution lengthened residence times.

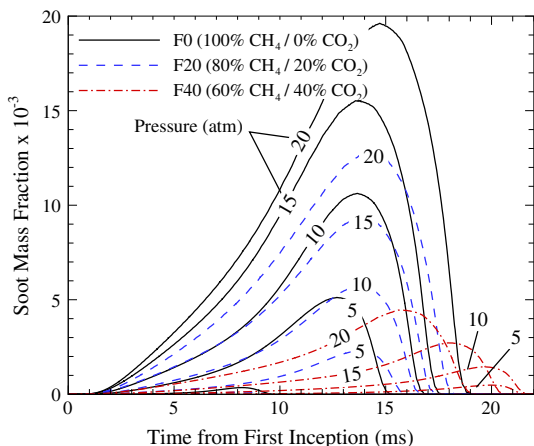


Fig. 16. Predicted soot mass fraction as a function of time along a soot particle trajectory. Particle trajectories start when soot formation began (i.e., soot concentrations rose above 0 ppm) and pass through the location of maximum soot concentration.

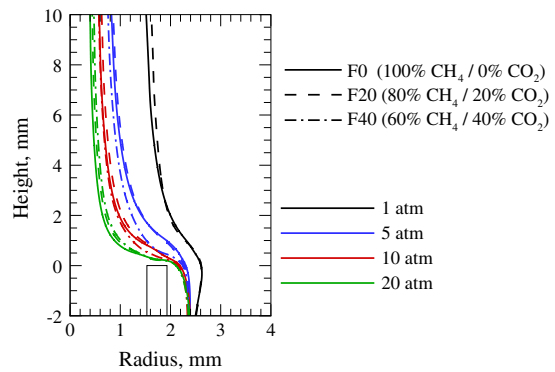


Fig. 17. Predicted soot particle trajectories. Particle trajectories pass through the location of maximum soot concentration.

Although there was little affect of pressure or dilution on the flame centerline velocity, as illustrated in Fig. 12, pressure and dilution both altered the overall soot residence times. This occurred because the soot particle trajectories, illustrated in Fig. 17, do not pass through the centerline. Rather, they began near the burner rim and moved inwards towards the centerline as soot traveled upwards. There was a small effect of dilution on the soot trajectories, but the effects of pressure were much stronger.

5. Summary and conclusions

Laminar diffusion flames burning simulated biogas fuels were investigated both experimentally and numerically to assess the influence of composition and pressure on flame structure and sooting propensity. Two different mixtures of methane and carbon dioxide were examined, with either 20% or 40% carbon dioxide by volume, and the results were compared with those for pure methane flames.

Generally, the numerical model predicted many of the experimentally observed trends with changes in pressure and/or dilution. However, there were some large discrepancies in the predicted temperatures and soot volume fractions, which were attributed to the acetylene-based soot model and uncertainties in the tube wall boundary conditions. Despite these errors, the predictions helped provide valuable insight into the behavior of the studied flames.

For pressures of 5 atm and above, the measured visible flame heights for all the flames were similar and were unaffected by changes in pressure or fuel CO₂ concentration. They were approximately 9 mm between 5 and 20 atm. The 1 atm flames were 1–2 mm shorter, depending upon the fuel. This was attributed to a lower core mass flow rate though the flame's envelope at lower pressures.

The numerical model was able to correctly predict these changes in flame height, or lack thereof, with changes in pressure and dilution. However, flame heights were over-predicted throughout the range of pressures considered. The predicted visible flame height was approximately 10 mm for all flames between 5 and 20 atm, compared to a measured value of 9 mm. Some small changes in visible flame height (between 1% and 5%) were predicted to occur that were not observed in the experiments.

The effects of pressure on soot formation in biogas diffusion flames were similar to those observed in other gaseous flames [14,21–24,26–28], i.e., soot yield increases with pressure. The measured soot yield in the biogas flames with 20% CO₂ dilution increased by about a factor of 1.9 when pressure was increased from 10 to 20 atm, and by a factor of 5.3 in the flames with 40% dilution. In comparison, soot yield only increases by a factor of

1.8 in the pure methane flames between 10 and 20 atm. Based on these results, the sensitivity of soot formation/destruction to pressure in biofuels showed a dependence on carbon dioxide concentration. In particular, fuels with higher CO₂ concentrations were found to be relatively more sensitive to pressure. The numerical model also predicted these trends, although the maximum soot yield in each flame was generally over-predicted. Predictions of the maximum carbon conversion factor were over-predicted by as much as 50% of the measured value.

Both the experimental and numerical results showed that diluting methane with carbon dioxide suppressed soot formation, and that the suppression effect of carbon dioxide was larger at lower pressures. At 10 atm, the measured carbon conversion factor was reduced by a factor of 14.4 when methane was diluted with 40% CO₂. The reduction in the carbon conversion factor with dilution was only a factor of 4.9 at 20 atm. In comparison, the mathematical model predicted a reduction by a factor of 6.8 and 4.3 at 10 and 20 atm, respectively.

The experimental and numerical results also indicated that the level of soot suppression at a fixed pressure varied linearly with carbon dioxide concentration. This linear relationship is mainly a result of the effects of dilution on chemical reaction rates, since the predicted maximum magnitudes of soot production and oxidation varied linearly with dilution. Surprisingly, the predicted overall lifetimes of soot particles along a particular path did not vary linearly with dilution as well. Rather, they showed a complex non-linear dependence on both pressure and dilution.

Acknowledgments

Financial support for the research described herein was provided by the Consortium for Research and Innovation in Aerospace in Quebec (CRIAQ), the Natural Sciences and Engineering Research Council (NSERC) in the form of a Collaborative Research and Development Grant, and Rolls-Royce Canada Inc. This funding is gratefully acknowledged with many thanks. Computational resources for performing all of the calculations reported herein were provided by the SciNet High Performance Computing Consortium at the University of Toronto and Compute/Calcul Canada through funding from the Canada Foundation for Innovation (CFI) and the Province of Ontario, Canada.

References

- [1] 2010 World Energy Outlook, International Energy Agency, 2010.
- [2] P.S. Nigam, A. Singh, *Prog. Energy Combust. Sci.* 37 (2011) 52–68.
- [3] H.N. Bhattia, M.A. Hanifa, M. Qasima, A. urRehmanb, *Fuel* 87 (2008) 2961–2966.
- [4] S. Rasi, A. Veijanen, J. Rintala, *Energy* 32 (2007) 1375–1380.
- [5] I.S. McLintock, *Combust. Flame* 12 (1968) 217–225.
- [6] K.P. Schug, Y. Manheimer-Timnat, P. Yaccarino, I. Glassman, *Combust. Sci. Technol.* 22 (1980) 235–250.
- [7] R.L. Axelbaum, C.K. Law, *Proc. Combust. Inst.* 23 (1991) 1517–1523.
- [8] Ö.L. Gülder, D.R. Snelling, *Combust. Flame* 92 (1993) 115–124.
- [9] I. Glassman, *Proc. Combust. Inst.* 27 (1998) 1589–1596.
- [10] K.C. Oh, H.D. Shin, *Fuel* 85 (2006) 615–624.
- [11] D.X. Du, R.L. Axelbaum, C.K. Law, *Proc. Combust. Inst.* 23 (1991) 1501–1507.
- [12] F. Liu, H. Guo, G.J. Smallwood, Ö.L. Gülder, *Combust. Flame* 125 (2001) 778–787.
- [13] C.E. Lee, S.R. Lee, J.W. Han, J. Park, *Int. J. Energy Res.* 25 (2001) 343–354.
- [14] F. Liu, K. Thomson, H. Guo, G.J. Smallwood, *Combust. Flame* 146 (2006) 456–471.
- [15] H. Guo, F. Liu, G.J. Smallwood, Ö.L. Gülder, *Proc. Combust. Inst.* 29 (2002) 2359–2365.
- [16] M.D. Smooke, M.B. Long, B.C. Connelly, M.B. Colket, R.J. Hall, *Combust. Flame* 143 (2005) 613–628.
- [17] H. Guo, G.J. Smallwood, *Combust. Sci. Technol.* 180 (2008) 1695–1708.
- [18] H. Guo, K.A. Thomson, G.J. Smallwood, *Combust. Flame* 156 (2009) 1135–1142.
- [19] J.D. Herdman, B.C. Connelly, M.D. Smooke, M.B. Long, J.H. Miller, *Carbon* 49 (2011) 5298–5311.
- [20] C.K. Law, G.M. Faeth, *Prog. Energy Combust. Sci.* 20 (1994) 65–113.
- [21] I.M. Miller, H.G. Maahs, *High-Pressure Flame Systems for Pollution Studies with Results for Methane-Air Diffusion Flames*, TN D-8407, NASA, 1977.
- [22] W.L. Flower, C.T. Bowman, *Proc. Combust. Inst.* 21 (1988) 1115–1124.
- [23] L.L. McCrain, W.L. Roberts, *Combust. Flame* 140 (2005) 60–69.
- [24] K.A. Thomson, Ö.L. Gülder, E.J. Weckman, R.A. Fraser, G.J. Smallwood, D.R. Snelling, *Combust. Flame* 140 (2005) 222–232.
- [25] H. GohariDarabkhani, J. Bassi, H.W. Huang, Y. Zhang, *Fuel* 88 (2009).
- [26] M.R.J. Charest, H.I. Joo, Ö.L. Gülder, C.P.T. Groth, *Proc. Combust. Inst.* 33 (2011) 549–557.
- [27] M.R.J. Charest, C.P.T. Groth, Ö.L. Gülder, *Combust. Flame* 158 (2011) 1933–1945.
- [28] M.R.J. Charest, C.P.T. Groth, Ö.L. Gülder, *Combust. Flame* 158 (2011) 860–875.
- [29] T.L.B. Yelverton, W.L. Roberts, *Combust. Sci. Technol.* 180 (2008) 1334–1346.
- [30] R.K. AbhinavamKailasanathan, T.L. Yelverton, T. Fang, W.L. Roberts, *Combust. Flame* 160 (2013) 656–670.
- [31] H.I. Joo, Ö.L. Gülder, *Proc. Combust. Inst.* 32 (2009) 769–775.
- [32] D.S. Bento, K.A. Thomson, Ö.L. Gülder, *Combust. Flame* 145 (2006) 765–778.
- [33] P.M. Mandatori, Ö.L. Gülder, *Proc. Combust. Inst.* 33 (2011) 577–584.
- [34] D.R. Snelling, K.A. Thomson, G.J. Smallwood, Ö.L. Gülder, E.J. Weckman, R.A. Fraser, *AIAA J.* 40 (2002) 1789–1795.
- [35] C.J. Dasch, *Appl. Opt.* 31 (1992) 1146–1152.
- [36] Ü.Ö. Köylü, G.M. Faeth, *J. Heat Transfer* 115 (1993) 409–417.
- [37] F. Xu, G.M. Faeth, *Combust. Flame* 125 (2001) 804–819.
- [38] S. Krishnan, K.-C. Lin, G. Faeth, *J. Heat Transfer* 122 (2000) 517–524.
- [39] K.C. Smyth, C.R. Shaddix, *Combust. Flame* 107 (1996) 314–320.
- [40] A.E. Karataş, G. Intasopa, Ö.L. Gülder, *Combust. Flame* 160 (2013) 1650–1656.
- [41] K.A. Thomson, *Soot formation in annular non-premixed laminar flames of methane-air at pressures of 0.1–0.4 MPa*, Ph.D. thesis, University of Waterloo, Waterloo, Ontario, Canada, 2004.
- [42] M.R.J. Charest, C.P.T. Groth, Ö.L. Gülder, *Combust. Theor. Model.* 14 (2010) 793–825.
- [43] K.M. Leung, R.P. Lindstedt, W.P. Jones, *Combust. Flame* 87 (1991) 289–305.
- [44] M. Fairweather, W.P. Jones, R.P. Lindstedt, *Combust. Flame* 89 (1992) 45–63.
- [45] F. Liu, H. Guo, G.J. Smallwood, Ö.L. Gülder, *J. Quant. Spectrosc. Radiat. Transfer* 73 (2002) 409–421.
- [46] J.O. Hirschfelder, C.F. Curtiss, R.B. Byrd, *Molecular Theory of Gases and Liquids*, John Wiley & Sons, New York, 1969.
- [47] A. Gomez, D.E. Rosner, *Combust. Sci. Technol.* 89 (1993) 335–362.
- [48] M.D. Smooke, C.S. McEnally, L.D. Pfefferle, R.J. Hall, M.B. Colket, *Combust. Flame* 117 (1999) 117–139.
- [49] M. Frenklach, H. Wang, *Springer Ser. Chem. Phys.* 59 (1994) 165–192.
- [50] J. Appel, H. Bockhorn, M. Frenklach, *Combust. Flame* 121 (2000) 122–136.
- [51] A. D'Anna, G. Mazzotti, J. Kent, *Combust. Sci. Technol.* 176 (2004) 753–767.
- [52] R.J. Hall, M.D. Smooke, M.B. Colket, in: F.L. Dryer, R.F. Sawyer (Eds.), *Physical and Chemical Aspects of Combustion: A Tribute to Irvin Glassman*, Gordon & Breach, Amsterdam, 1997, pp. 189–230.
- [53] A. D'Anna, J.H. Kent, *Combust. Flame* 152 (2008) 573–587.
- [54] Q. Zhang, H. Guo, F. Liu, G.J. Smallwood, M.J. Thomson, *Combust. Theor. Model.* 12 (2008) 621–641.
- [55] J.S. Sachdev, C.P.T. Groth, J.J. Gottlieb, *Int. J. Comput. Fluid Dyn.* 19 (2005) 159–177.
- [56] S.A. Northrup, C.P.T. Groth, *Solution of laminar diffusion flames using a parallel adaptive mesh refinement algorithm*, in: 43rd AIAA Aerospace Sciences Meeting and Exhibit, Reno, Nevada, 2005. AIAA paper 2005-0547.
- [57] S.A. Northrup, C.P.T. Groth, *Solution of laminar combustions flows using a parallel implicit adaptive mesh refinement algorithm*, in: *Proceedings of the Fourth International Conference on Computational Fluid Dynamics, ICCFD4*, Ghent, Belgium, 2006, pp. 341–346.
- [58] X. Gao, C.P.T. Groth, *Int. J. Comput. Fluid Dyn.* 20 (2006) 349–357.
- [59] X. Gao, S. Northrup, C.P.T. Groth, *Prog. Comput. Fluid Dyn.* 11 (2011) 76–95.
- [60] P.L. Roe, *J. Comput. Phys.* 43 (1981) 357–372.
- [61] W.J. Coirier, K.G. Powell, *AIAA J.* 34 (1996) 938–945.
- [62] J.M. Weiss, W.A. Smith, *AIAA J.* 33 (1995) 2050–2057.
- [63] B.G. Carlson, K.D. Lathrop, in: H. Greenspan, C.N. Kelber, D. Okrent (Eds.), *Computing Methods in Reactor Physics*, Gordon and Breach, London, 1968, pp. 171–266.
- [64] C.P. Thurgood, A. Pollard, H.A. Becker, *J. Heat Transfer* 117 (1995) 1068–1070.
- [65] F. Liu, G.J. Smallwood, Ö.L. Gülder, *J. Thermophys. Heat Transfer* 14 (2000) 278–281.
- [66] F. Liu, G.J. Smallwood, Ö.L. Gülder, *J. Quant. Spectrosc. Radiat. Transfer* 68 (2001) 401–417.
- [67] D.G. Goodwin, *Chem. Vapor Depos.* XVI and *EUROCVI* 14 (2003) 155–162.
- [68] G.P. Smith, D.M. Golden, M. Frenklach, N.W. Moriarty, B. Eiteneer, M. Goldenberg, C.T. Bowman, R.K. Hanson, S. Song, W.C. Gardiner Jr., V.V. Lissianski, Z. Qin, *Gri-mech 3.0*, 2002. <http://www.me.berkeley.edu/gri_mech/>.
- [69] H. Guo, F. Liu, G.J. Smallwood, Ö.L. Gülder, *Combust. Theor. Model.* 6 (2002) 173–187.
- [70] Ö.L. Gülder, K.A. Thomson, D.R. Snelling, *Combust. Flame* 144 (2006) 426–433.
- [71] S.A. Skeen, G. Yablonsky, R.L. Axelbaum, *Combust. Flame* 156 (2009) 2145–2152.
- [72] F.G. Roper, *Combust. Flame* 29 (1977) 219–226.
- [73] F.G. Roper, C. Smith, A.C. Cunningham, *Combust. Flame* 29 (1977) 227–234.
- [74] A.E. Karataş, Ö.L. Gülder, *Prog. Energy Combust. Sci.* 38 (2012) 818–845.
- [75] G. Rudinger, *Fundamentals of Gas-Particle Flow*, Elsevier Scientific, 1980.